Open Ceramics 10 (2022) 100253

Contents lists available at ScienceDirect

Open Ceramics

journal homepage: www.sciencedirect.com/journal/open-ceramics

Mobile sealing and repairing of damaged ceramic coatings by powder aerosol deposition at room temperature

Mario Linz *, Jörg Exner, Tobias Nazarenus, Jaroslaw Kita, Ralf Moos

University of Bayreuth, Department of Functional Materials Universitätsstraße 30, 95440, Bayreuth, Germany

ARTICLE INFO

Keywords:
Aerosol deposition method (ADM)
Room temperature impact consolidation (RTIC)
Ceramic spray coating

ABSTRACT

Repair instead of discard is going to be crucial in the vision of a green future, therefore we propose the powder aerosol deposition (PAD) as a promising technique to reprocess ceramic coatings at room temperature. Alumina coated copper substrates with an artificial imperfection are manufactured in a first step. In a second step, the repair of this imperfection is carried out using two different PAD apparatuses: first, a conventional PAD apparatus with a moving substrate holder and a converging slit nozzle and second, a miniaturized μPAD apparatus with a fixed substrate holder and a circular de-Laval nozzle. The different film profiles are studied using a laser scanning confocal microscope. Cross-sectional images to investigate the microstructure are taken by a scanning electron microscope. Finally, samples of both PAD apparatuses are exposed to an oxidizing atmosphere at 400 °C proving the gas-tightness as a further quality feature of the repair coating.

1. Introduction

Ceramic films are of high interest in a broad variety of technical applications, ranging from thermal barrier coatings, abrasive and chemically stable protective films over electrically insulating films to applications as functional components in electronic devices, solid oxide fuel cells, lithium-ion batteries or sensors. It is a major drawback for many ceramic films that typically very high production temperatures (>1000 °C) either during or after film formation are required to form the dense and suitable ceramic (micro)morphology. Two exemptions exist that may overcome this requirement: cold sintering [1] and aerosol deposition method [2]. While the first technique is mainly utilized to manufacture bulk samples [3], the latter enables to produce dense ceramic films without any heat treatment directly at room temperature [4]. Aerosol Deposition (abbreviated as AD or ADM) [5] is a dry ceramic powder spray coating method that uses micrometer-sized powders (mean particle diameter in the range of 0.2–5 μm) [2]. However, process descriptions like Powder Aerosol Deposition (PAD [6], to avoid confusion with solvent-based spray processes), Vacuum Kinetic Spray (VKS) [7], Vacuum Cold Spray (VCS) [8], Nano Particle Deposition System (NPDS) [9], or Granule Spray in Vacuum (GSV) [10] are oftentimes used for this technique depending on the research group and region. Dry ceramic powders are accelerated to velocities of several hundred m/s in a carrier gas flow of 1–20 L min^{-1}. The particles subsequently collide with the surface that is to be coated in low vacuum conditions ($p \approx 1$ mbar). Film formation and film growth occur according to the Room Temperature Impact Consolidation mechanism (RTIC) by mainly using the kinetic energy of the impacting particles without dominating thermal heating effects [11]. Due to the high-momentum upon impact with the substrate, the particle undergoes a brittle fragmentation along grain boundaries as well as through grains in conjunction with plastic lattice deformation [12]. The newly formed nanometer-sized fragments exhibit fresh, unsaturated, and therefore reactive surfaces that may play an important role for the strong adhesion of the film to the substrate as well as to the already deposited particles. An additional film densification, the so-called hammering effect, emerges by subsequently impacting particles that consolidate the previously formed film. A more detailed description of the aerosol deposition process, its deposition mechanism, and the resulting film properties can be found in overview articles of Akedo's group [13,14] and of our group [2].

Several previous publications report on protective films formed by PAD, like oxidation resistant coatings for metallic interconnects made of $(La_{0.8}Sr_{0.2})_{0.98}MnO_3$ [15,16], $MnCo_2O_4$ [17], or $LaNiO_3$ [18]. Furthermore, corrosion protection films of YSZ [19], as well as wear-resistant films of Al_2O_3 [20,21] or ZnS/nanodiamond [22], or even exotic ones like extraterrestrial regolith [23,24] are reported.

Technological developments in PAD mainly point towards a better understanding of the deposition mechanism [12,25–28], and a scale-up

* Corresponding author.
E-mail address: Functional.Materials@Uni-Bayreuth.de (M. Linz).

https://doi.org/10.1016/j.oceram.2022.100253
Received 16 February 2022; Accepted 5 April 2022
Available online 8 April 2022

of the spray process [29]. The latter resulted in an enhanced process control and increased coating areas [29,30]. In a complimentary approach, we recently demonstrated that PAD is also possible at a significantly reduced device size and complexity when using single spot deposition and miniaturized deposition chambers (Micro Powder Aerosol Deposition, μPAD) [31,32]. This operation mode in particular enables the use of semi-open vacuum deposition chambers that are sealed by directly placing the chamber opening on the surface to be coated. Consequently, the size of the sample/item is not limited by the inner dimensions of the coating chamber since it is located outside of it – the sample in fact serves as a wall of the coating chamber. In addition to initially form ceramic films on previously uncoated surfaces, this also makes it possible to easily repair damaged ceramic coatings at room temperature with any ceramic material that can be deposited by PAD. Maintenance times and costs may drastically be lowered as a reprocessing of the damaged coating is achieved directly at room temperature and even in a fully assembled state (as long as the part is directly accessible by the miniaturized deposition chamber). This eliminates the typical effort and expenses of disassembly, parts transport, extensive cleaning, batch oven runs, quality control, and subsequent reassembly.

In this work, we shed some light on this opportunity to repair ceramic coatings using μPAD with single spot deposition and semi-open deposition chambers. The experiments are performed on copper substrates with a partially damaged spot in the previously applied alumina protection PAD-film. An uncovered part of the substrate with a diameter of 5 mm, denoted in the following as "artificially damaged spot" or just "hole", will be subsequently coated with alumina by μPAD and PAD, respectively, and the samples are subsequently placed in oxidizing atmospheres at elevated temperatures to determine the oxidation resistance of the reprocessed coating. The samples are characterized by SEM imaging and by three-dimensional surface profile measurements. The results are compared with conventionally processed PAD films as well as with samples with an uncovered artificial imperfection. Our main objective is to analyze the suitability of μPAD as well as conventional PAD to repair damaged ceramic films by using exemplarily alumina (oxidation) protection films.

2. Experimental details

Rectangular blank copper substrates (area of 2×1 cm^2 and thickness of 0.5 mm) with an attached handlebar were used for the coating experiments. The sample preparation is in generally divided in two steps: (I) preparation of the initial alumina film excluding the intended artificially damaged spot and (II) sealing/covering the artificially damaged spot by powder aerosol deposition, here either by conventional PAD (II-a) or μPAD (II-b). For all coating runs (μPAD as well as PAD), the identical alumina powder from Sasol Chem. with an average particle size of $d_{50} = 0.9$ μm was used after it had been sieved (mesh 90 μm) and dried at 200 °C for at least 48 h.

First, the initial alumina film is applied by conventional aerosol deposition (PAD) as presented in the scheme in Fig. 1a. In order to create the artificially damaged area as a "bad spot" for the later reprocessing, a circular Kapton® mask with a diameter of about 5 mm was applied to the center of the substrate before PAD to avoid any film deposition in this area. Consequently, the formed alumina film shows a hole after removing the Kapton® mask (sample denoted as type I).

The coating process was conducted in a custom-made PAD device as described in Ref. [2] using the spray parameters in Table 1. Further details of the film morphology like detailed film thickness and SEM images as well as surface roughness values of sample type I are given in section 3.

The previously formed artificially damaged spot (hole) from type I was subsequently covered by two different approaches to investigate their suitability to repair damaged coatings. In the first attempt, conventional PAD including a scanning movement of the sample was utilized as depicted in Fig. 1b (denoted as type II-a). This mode is identical

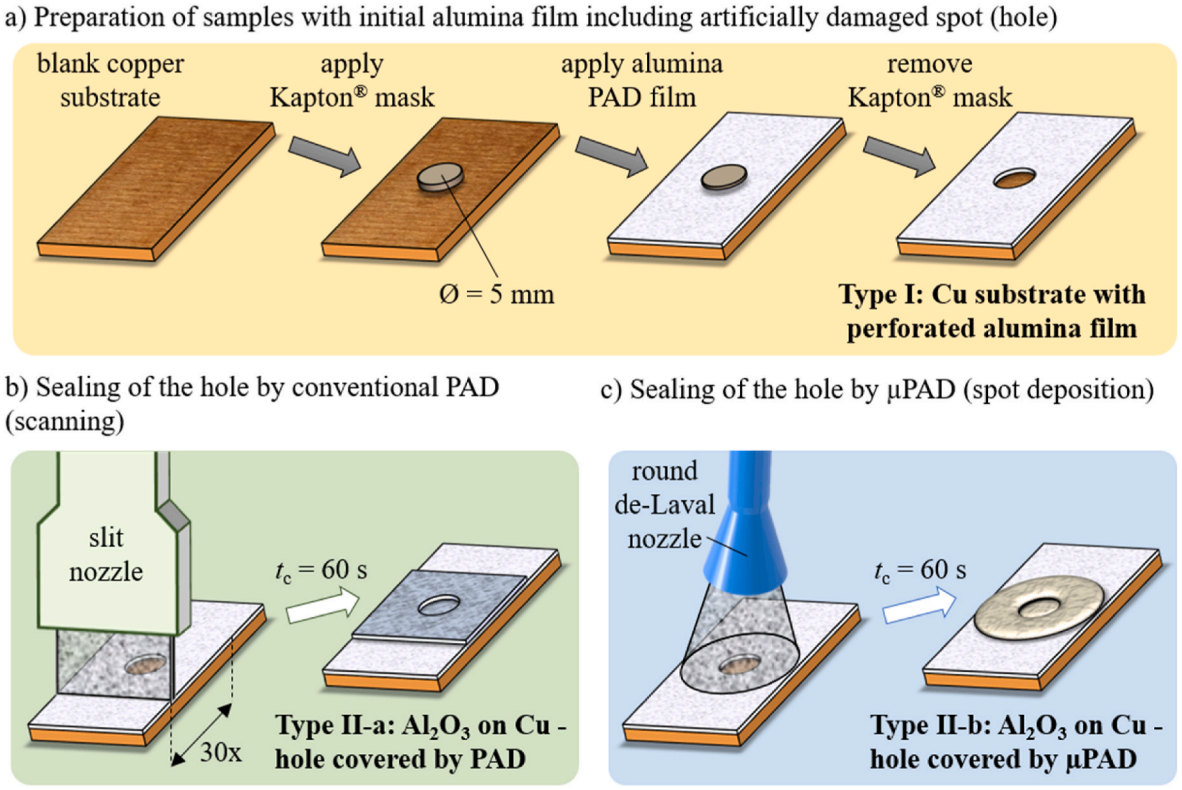

Fig. 1. Scheme of preparation methods: a) formation of the initial alumina film by PAD including a hole formed by masking the deposition area, b) sealing of the hole by conventional PAD, and c) sealing of the hole by μPAD spot deposition.

Table 1
Spray parameters used conventional PAD to build the initial alumina film (type I).

sample type I	conventional PAD
aerosol generation unit	custom-built fluidized bed aerosol generator
Nozzle	converging slit nozzle, orifice: 25 mm × 0.4 mm
distance nozzle - substrate	2 mm
carrier gas flow	8 L min^{-1} O_2
pressure aerosol chamber	200 mbar
pressure deposition chamber	<1 mbar
substrate scan velocity	5 mm s^{-1}
duration of coating t_c	120 s (60 scans) per sample
film area per sample	rectangular, 25 mm × 10 mm
substrate masking	circular Kapton® mask (Ø = 5 mm)
coating material	Al_2O_3 powder (Sasol Chem., d_{50} = 0.9 µm, sieved and dried)
substrate material	blank copper substrate (R_a = 0.40 µm, R_z = 2.2 µm)

to the method used to form the initial alumina film; however, the used process parameters were slightly adjusted to the smaller coating area. Here, a rectangular area of 10 mm by 10 mm was coated over the circular hole positioned in the center (Fig. 1b). Main differences to the film deposition of type I were the smaller slit nozzle width of 10 mm and the therefore adapted carrier gas flow of 6 L min^{-1} as well as the halved number of scans of 30 (see Table 2). Additionally, since the sample is only partially coated at this stage, the turning points of the scanning movement had been masked to achieve a homogeneous film.

In a different approach, the hole was sealed using the previously introduced single-spot µPAD setup as described in Ref. [31] featuring a less complex coating device, lowered areal footprint (30 cm × 20 cm, excluding the vacuum pump) and significantly simplified handling (see Fig. 2).

For the µPAD, one part of the total gas flow is used to aerosolize the ceramic particles while the other part is used to dilute and accelerate the particle-laden aerosol afterwards. The splitting of the gas flows and their subsequent merge are necessary for two reasons: first, an identical aerosol gas flow like for conventional PAD (type II-a) as an increased gas flow through the aerosol chamber empties it too fast and second, a minimum gas flow is required to have the de-Laval nozzle work properly. Apart from the moving or stationary substrate mounting respectively, the use of a de-Laval nozzle is the second main difference between the conventional PAD and µPAD as illustrated in Fig. 3.

Table 2
Spray parameters used to cover the hole by PAD (type II-a), and by µPAD (type II-b).

	conventional PAD (type II-a)	µPAD (type II-b)
aerosol generation unit	custom built fluidized bed aerosol generator	
Nozzle	converging slit nozzle orifice: 10 mm × 0.5 mm	de-Laval-type round nozzle orifice: Ø = 10 mm throat: Ø = 3.5 mm
distance nozzle - substrate	2 mm	55 mm
carrier gas flow	6 L min^{-1} O_2	6 L min^{-1} O_2 (aerosol unit) +2 L min^{-1} O_2 (dilution)
pressure aerosol chamber	210 mbar	210 mbar
pressure deposition chamber	<1 mbar	1.4 mbar
substrate scan velocity	5 mm s^{-1}	none – spot deposition
duration of coating t_c	60 s (30 scans)	60 s
film area	rectangular, 10 mm × 10 mm	circular, bell-shaped profile Ø ≈10 mm (FWHM)
substrate masking	turning points of scanning	none
coating material	Al_2O_3 powder (Sasol Chem., d_{50} = 0.9 µm, sieved and dried)	
Substrate	samples type I (perforated alumina film on copper)	

For better comparability of type II-a and type II-b sample, the duration of coating t_c was set to identical values of 60 s for both setups: the 30 scans for type II-a are therefore the result from a scanning area of 10 mm with a substrate scan velocity of 5 mm s^{-1} over a period of 60 s.

In order to prove the gas tightness as a key feature of PAD films, all samples of type I, type II-a, and type II-b were heated altogether up to 400 °C in a muffle furnace and held for a dwell time of 5 h at peak temperature before cooling. Surrounding ambient air with a relative humidity of about 60% was allowed to pass the muffle furnace by natural convection. The uncoated part of the Cu substrate shall oxidize to CuO and form a visible black surface while the coated part should remain unaffected by the oxidation and retain its coppery gloss.

The analyses of all films were carried out using a laser scanning confocal microscope (LSM, Zeiss LSM900, Oberkochen, Germany) for the three-dimensional surface topography as well as for the film thickness measurements and a scanning electron microscope (SEM, Zeiss Leo 1530, Oberkochen, Germany) was used for the cross-sectional images.

3. Results and discussion

A homogeneous, well-adhering spot coating is the goal of the repair procedure. Therefore, the interface between the repair coating and the initial alumina film as well as the interface between the repair coating and the artificial imperfection (hole, i.e., blank Cu substrate) are studied in detail. A dense ceramic film with no signs of delamination, especially at the transition point from initial coating to the artificial imperfection, is considered crucial. The surface morphology characterization starts with the blank Cu substrate followed by samples with initial coating (type I) as well as reprocessed surfaces (type II-a and type II-b, respectively), all in the non-oxidized state. Subsequently, film microstructure after oxidation is discussed based on cross-sectional SEM images.

3.1. Surface and profiles of films

Fig. 4 shows the different steps of the sample preparation. The blank copper substrate in Fig. 4a exhibits a textured surface (vertical stripes) depicting its roll direction during previous reshaping. In the first step, the initial PAD alumina film with a thickness of 3 µm (see Fig. 5b for the film thickness) was formed excluding the masked center of the sample (Fig. 4b).

Here, the coated area appears opaque with a grayish color due to the lowered reflectivity compared to the blank copper surface which is still visible in the uncoated center of the sample. Between coated and uncoated region, a distinctive and well-defined edge in the shape of the perimeter of the previously attached Kapton® mask exists. The repaired samples before oxidization are shown in Fig. 4c and d. The previously exposed blank copper within the perimeter of the hole shows a uniform coating with lowered reflectivity after the second PAD and µPAD processing, respectively, similar to the observations for the initial alumina coating.

Fig. 5 shows the surface profiles, taken by a laser scanning confocal microscope before and after the initial coating with alumina.

Fig. 5a shows the three-dimensional representation of the blank Cu substrate surface with the described texturing in form of a distinctive roughness. Along the white arrow, the substrate's surface profile is extracted in the middle of the substrate exhibiting a roughness of R_a = 0.40 µm and R_z = 2.2 µm.

The sample after an initial coating with alumina (type I) is shown in Fig. 5b. The distinct circular hole in the middle of the Cu substrate originates from the Kapton® masking. The height difference from this artificial imperfection to the initial alumina film is about 3 µm. In contrast to the blank Cu substrate, a slightly higher surface roughness of the alumina film of R_a = 0.67 µm and R_z = 4.51 µm can be noticed by comparing both film profiles.

Fig. 6 shows the surface profiles of the covered holes with the

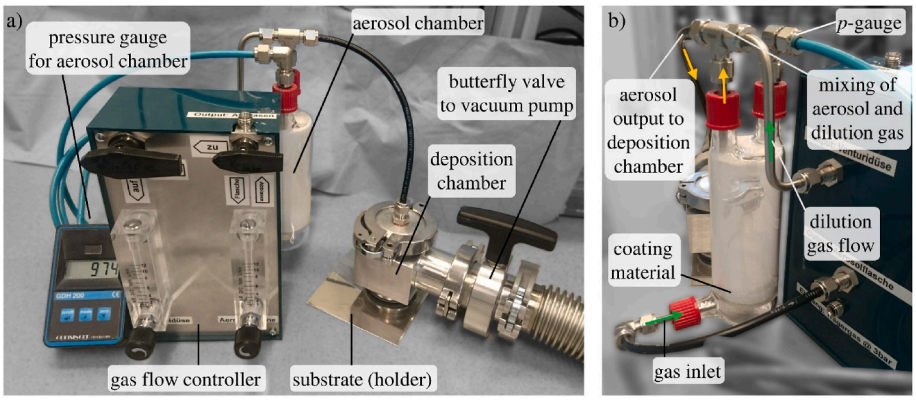

Fig. 2. Image of the used modular µPAD apparatus with single-spot deposition: a) front view of the complete setup and b) back view depicting the aerosol chamber and the aerosol-/gas flows (green arrows indicate gas flows while yellow arrows indicate aerosol transport) from Ref. [31] with permission of the authors. (For interpretation of the references to color in this figure legend, the reader is referred to the Web version of this article.)

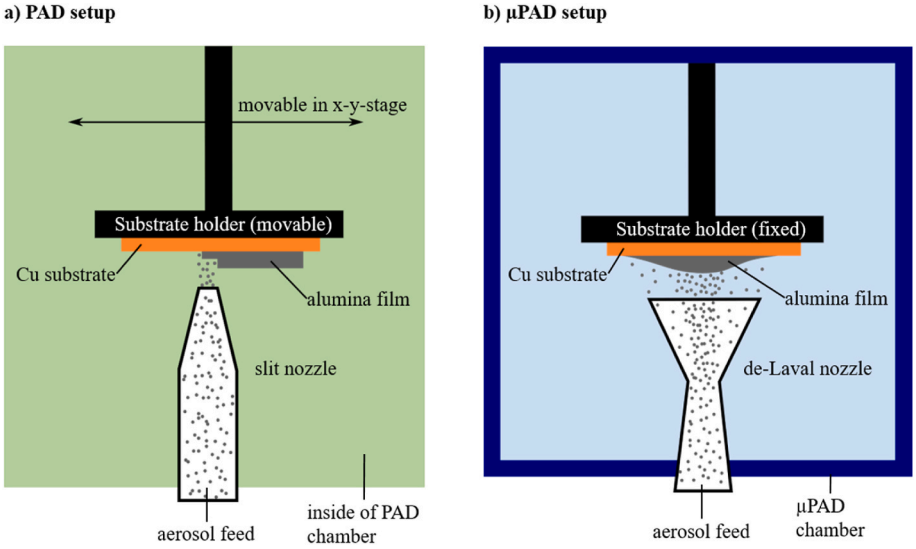

Fig. 3. Schematic representation of both spray setups used in this study: a) conventional PAD and b) µPAD. Shown are only the sections with nozzle, formed aerosol jet, substrate, and substrate mounting.

conventional PAD and the µPAD respectively.

The covered hole using the conventional PAD (type II-a) and µPAD (type II-b) are shown in Fig. 6a and b, respectively. Both samples exhibit a completely repaired imperfection. Fig. 6a shows a sharp edge at the repaired imperfection with a film height of 3 µm measured to the initial alumina layer. Nevertheless, the circular spot in the middle of the sample can clearly be localized as the film on the imperfection is lower than its surroundings. This behavior is typical for aerosol deposition since the applied film approximately follows the underlying surface. For example, the roughness of the copper substrate is still visible even after applying two PAD films on top of each other, each with a thickness of about 3 µm (region outside of the previous imperfection).

Compared to the conventional PAD, the µPAD sample shows no sharp rim (see Fig. 6b) at the edges of the repair coating as a masking at the turning points was not necessary. The shape of the film is significantly different from the conventional PAD: instead of a sharp edge and a clear visibility of the imperfection, a moderate slope at the edges with a plateau in the middle is formed. It appears that the µPAD fills up the imperfection and the formed coating looks like a heap over it. In contrast to type II-a, the type II-b coating seems to resemble to the underlying structure to a smaller extent, since the imperfection in the center of the initial alumina layer cannot be distinguished anymore. Nevertheless, the substrate texturing still appears at the surface of µPAD film.

Subtracting the film profile of type I from the profile of type II-a and type II-b leads to the profiles shown in Fig. 6c and d, respectively, that demonstrate the contribution of solely the reprocessing stage to the total film thickness. The repaired film produced by the conventional PAD shows a homogeneous profile of about 3–4 µm in film thickness in the middle and a slight camber at the edges ($y = 0$ mm and $y = 9$ mm). Type II-b coating produced by µPAD in contrast leads to a bell-shaped film profile with a maximum film thickness of 8–9 µm. The film thickness shows a slope at the starting point where the maximum is reached after 6 mm, followed by a plateau of 4 mm with maximum film thickness. A second slope decreasing the film thickness over a length of 6 mm follows hereinafter. While the contribution of the conventional PAD film in Fig. 6c exhibits a nearly flawless shape with constant film thickness build-up, the µPAD film contains some regions with a sudden drop in the film thickness that significantly deviate from the bell-shape. These regions are located around the perimeter of the imperfection ($x = 6$ mm and $x = 12$ mm, respectively), indicating that some challenges may arise for the film formation in case of the used µPAD spot deposition. Yet, at no point, the observed film profile reaches values below 3 µm, meaning that even for the most pronounced film thickness drops at least a protective film of 3 µm in thickness is present. Since the thickness does not fall below the initial film, this circumstance should not limit the proper function and lifetime of the reprocessed coating. Nevertheless, the repair

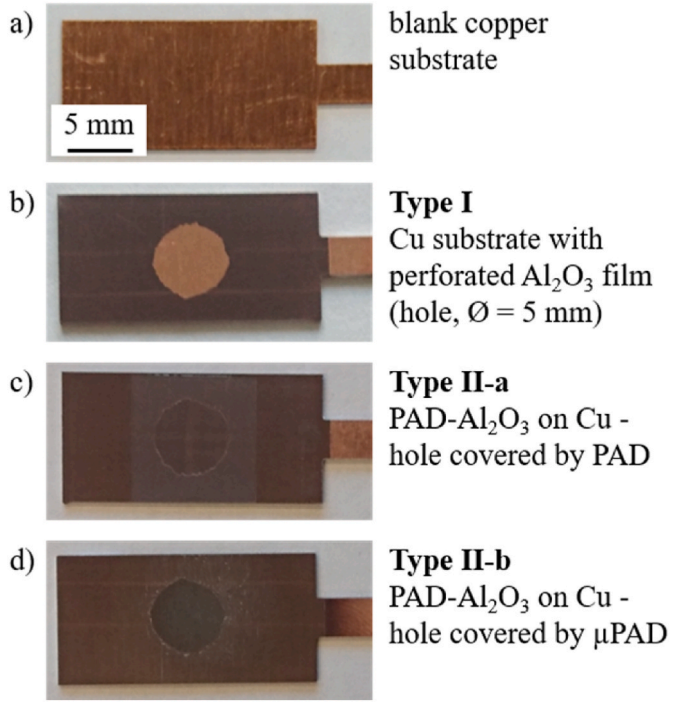

Fig. 4. Image of the samples at different manufacturing steps: a) blank copper, b) coated with the initial PAD alumina film excluding a hole in the center (type I), c) hole covered by conventional PAD (type II-a), and d) hole covered by µPAD (type II-b).

coating formed by conventional PAD seems less affected from the transition "initial coating – hole" than the one formed by µPAD.

The general differences in the shape of the profiles originate from the different nozzles (slit nozzle for the conventional PAD and de-Laval nozzle for the µPAD). While the converging slit nozzle leads to an even coating as particles are distributed uniformly over the nozzle outlet within the *y*-direction and by the continuous scanning movement within the *x*-direction, a de-Laval nozzle consists of a converging and diverging part. The critical diameter (smallest diameter in the nozzle) of the used de-Laval nozzle is 3.5 mm, which correlates very well to the plateau-like area of the profile measuring 4 mm in diameter. As all particles have to pass the critical diameter, a bell-shaped particle distribution over the cross-section of the nozzle is given. The total diameter of the µPAD spot coating is about 16 mm, which deviates from the nozzle's orifice of 10 mm. We assume a beam expansion that leads to the larger coated area.

3.2. Oxidation test

Fig. 7 shows the results of the thermal treatment at 400 °C of all samples described in section 2 (type I, type II-a, and type II-b).

All samples show an oxidation from Cu to CuO at the uncoated handlebar on the right side (also acting as thermal treatment indicator). Type I shows additional oxidation of the artificial imperfection within the uncoated (previously masked) region. The surrounding initial alumina film is gas-tight and the substrate keeps its metallic appearance. Type II-a shows a whitish, opaque film surrounding the imperfection while for the imperfection itself, the metallic shine remains. The reduced translucence is a result of the higher film thickness surrounding the imperfection (see Fig. 6a) [33]. The circular coating of type II-b can be identified by the brownish curved edges left and right to the imperfection. The coating of the imperfection of type II-b is opaquer compared to type II-a, a result from the higher film thickness. The white sparkles of the type II-b coating originate from a higher surface roughness. Both coating methods, as used for type II-a and type II-b, enable the formation of a gas-tight film and therefore achieving the set requirement for the oxidation protecting coating. Apart from the reduction in the translucence, which is a result of the increased film thickness, no indication of the oxidation of the artificial imperfection can be found.

3.3. Film morphology

Fig. 8 shows the cross-sectional SEM images in different preparation steps for the type I sample: from the blank Cu substrate to the initially coated and perforated alumina film.

Fig. 8a–c shows the cross-sectional SEM images of the blank Cu substrate in different magnifications. The embedding resin appears dark gray at the top of Fig. 8a while the Cu substrate is visible in lighter gray at the bottom. The horizontal lines at higher magnification within the Cu substrate originate from the polishing steps of the SEM sample preparation. Fig. 8d–f shows the initial alumina film (type I) in different magnifications at in the middle of the film denoted as SEM spot 1 (see Fig. 8i). A dense and well-adhering Al_2O_3 film is formed. Gaps, pores, and detachments are not found between the film and the substrate nor within the film itself. The edge of the artificial imperfection is resolved in Fig. 8g and h in different magnifications (SEM spot 2). The alumina

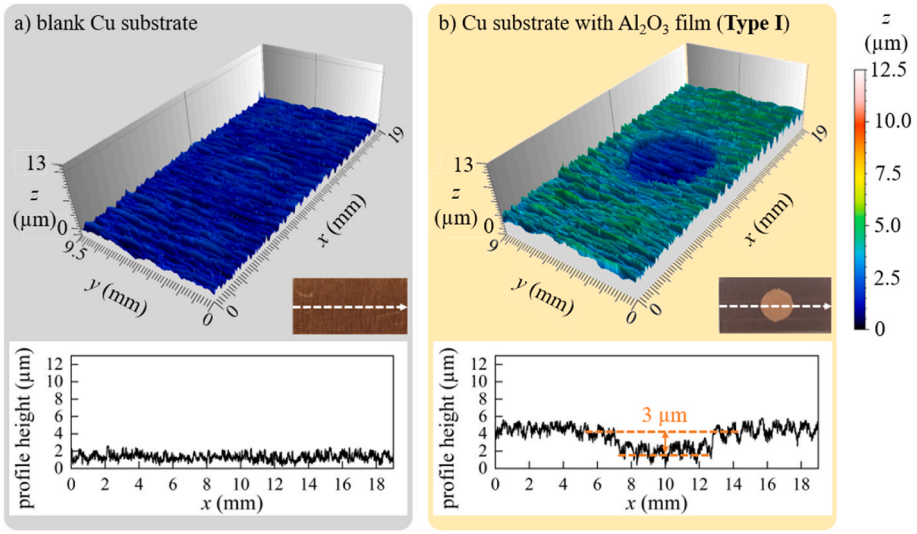

Fig. 5. Surface profiles taken by laser scanning confocal microscopy of a) the blank copper substrate and b) after applying the initial alumina film using masked PAD (Type I). Line profiles were extracted in direction of the arrow.

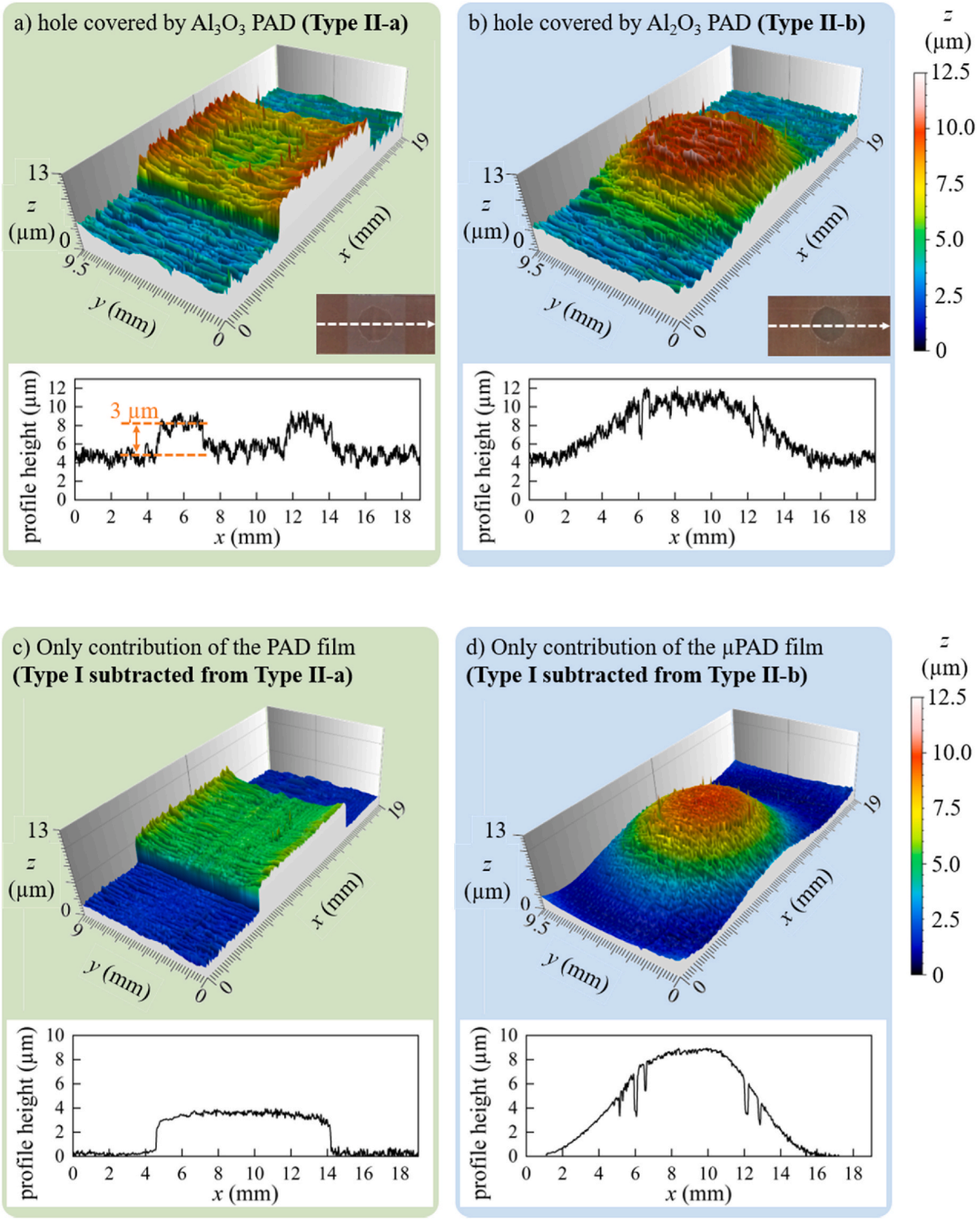

Fig. 6. Surface profiles taken by laser scanning confocal microscopy of a) the coated artificial imperfection (hole) using the conventional PAD (type II-a) and b) using the µPAD (type II-b). The sole contribution of the reprocessing step to the film thickness (type I's surface subtracted from the surface of the sample type II-a as well as type II-b) are shown in c) and d), respectively. Line profiles were extracted in direction of the arrow.

film decreases its thickness over a short length of 60 µm (Fig. 8g) and comes to a well-defined stop (Fig. 8h). At the end of the hole, the initial alumina film shows the same good adherence as on the previous SEM spot 1.

Fig. 9 shows the type I sample after oxidation at 400 °C at two different spots: the initial alumina film and the oxidized Cu in the center of the hole.

Fig. 9a–c shows the initial alumina coating (type I) after the oxidation at 400 °C in different magnifications at the SEM spot 1 (see Fig. 9f). Even after the thermal treatment, the film shows no pores, no detachments and still exhibits a good adhesion to the Cu substrate. In contrast to the well-adhering alumina film, the oxidized Cu (CuO) at the center of the hole (SEM spot 2) shows a large horizontal crack and a delamination from the blank Cu substrate occurs (Fig. 9d-**e**). Furthermore, pores in the CuO can clearly be noticed as darker spots within the detached layer. Presumably, void formation at the interface of the

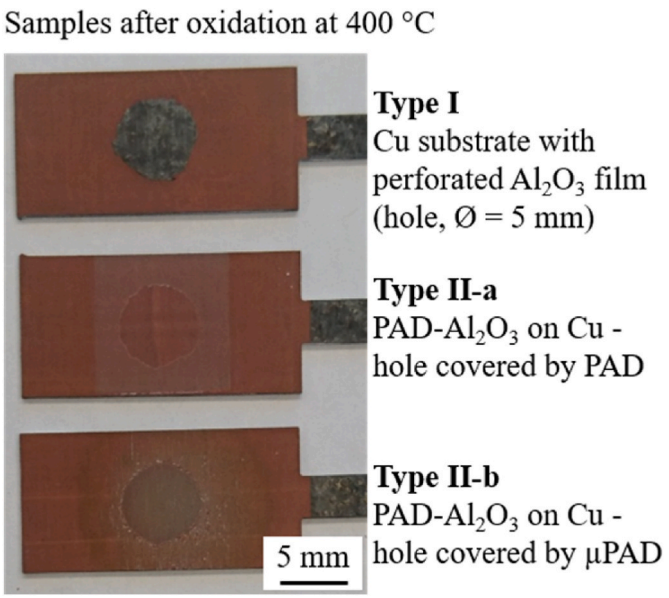

Fig. 7. Images of samples after oxidation at 400 °C in ambient laboratory atmosphere: hole not covered (type I) or covered by conventional PAD (type II-a) and µPAD (type II-b), respectively.

growing copper oxide film to the copper substrate led to a film peel-off in accordance to Ref. [34]. The low adhesion of the formed oxide film could also be observed at the handle bars where the dark copper oxide is prone to flaking even at low mechanical stresses when touched with a nitrile glove.

Fig. 10 shows the SEM images at two different spots (see Fig. 10f) of the type II-a sample (conventional PAD).

Fig. 10a–c shows the starting edge of the PAD repair coating on the initial PAD film (SEM spot 1) after oxidation at 400 °C in different magnification. Due to the seamless bonding of the repair coating to the underlying initial alumina film, not resolvable by SEM, a dashed line as a guide-for-the-eye is added. The repair coating is of such high quality that only the increase in the film thickness indicates the starting point of the second deposition.

Similar to the starting point of the repair coating, a decrease in the film thickness at the edge of the artificially damaged spot (see Fig. 10d-e) marks the coating of the artificial imperfection (SEM spot 2). Again, a dashed line is added as a guide-for-the-eye to indicate both coatings. The initial hole as well as the edge towards the initial PAD film are fully covered by the second film, without any gaps nor pores or delamination. Instead, a seamless transition of the repair film over the edge of the hole is observed. The latter is crucial to achieve the necessary oxidation protection. In contrast to the oxidized sample I, it is remarkable that no signs of oxidation flaws like void formation or flaking are visible although this sample was heat treated at 400 °C, too. This underlines the capability of PAD films to form gas-tight ceramic films not only on flat surfaces but also in regions with transitions from uncoated substrates to preexisting films.

Fig. 11 shows the repair coating manufactured by the µPAD (type II-b).

Unlike the type II-a sample, only a single SEM spot is analyzed (see

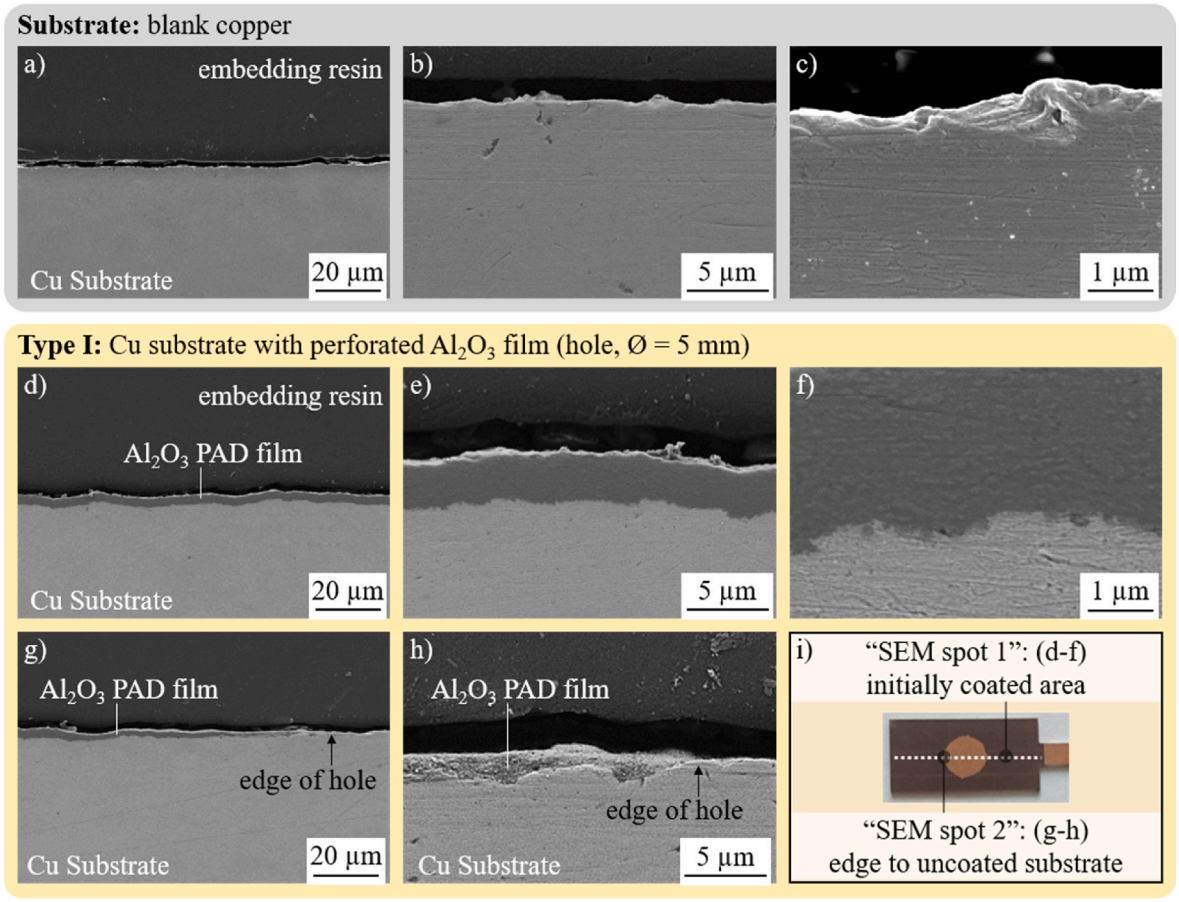

Fig. 8. Cross-sectional images taken by SEM of a) – c) the used blank Cu substrate without coating, and after applying the initial alumina film by PAD: d) – f) at "SEM spot 1" in the middle of the film and g) – h) at "SEM spot 2" at the edge to the uncoated substrate. The cross-sectional images are taken at different magnifications: images vertically arranged one above the other use identical magnifications. A top view of the sample, marked with the different SEM spots, is shown in i).

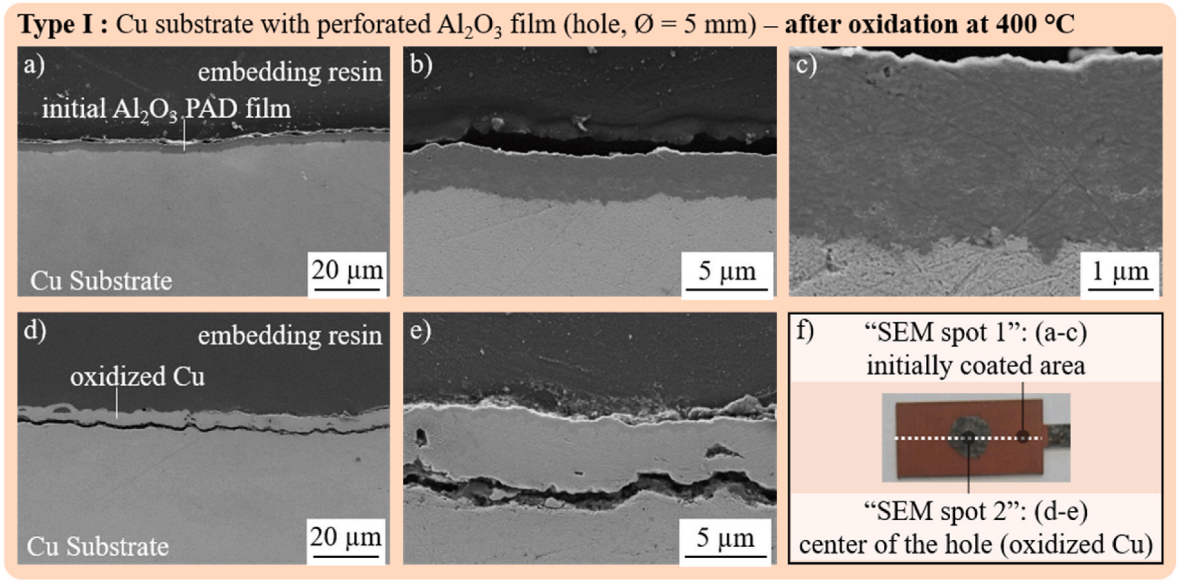

Fig. 9. Cross-sectional images of the oxidized sample taken by SEM of a) – c) the initial alumina coating at "SEM spot 1" and d) – e) the artificial imperfection at "SEM spot 2". The cross-sectional images are taken at different magnifications: images vertically arranged one above the other use identical magnifications. A top view of the sample, marked with the different SEM spots, is shown in f).

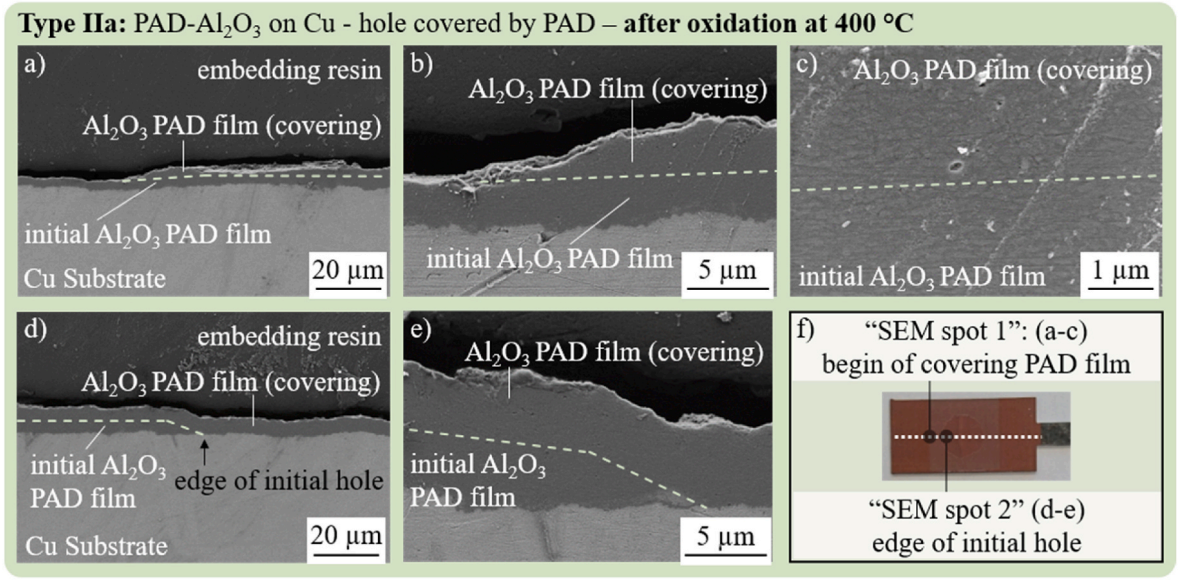

Fig. 10. Cross-sectional images of the oxidized type II-a sample taken by SEM of a) – c) "SEM spot 1" at the begin of the PAD repair coating on the initial PAD coating and d) – e) "SEM spot 2" at the edge to the initial hole. The cross-sectional images are taken in different magnifications: images vertically arranged one above the other use identical magnifications. The dashed line is a guide-for-the-eye to distinguish between initial PAD film and covering PAD film. A top view of the sample, marked with the different SEM spots, is shown in f).

Fig. 11a) because the bell-shaped repair coating over the artificially damaged spot allows no localization of the edge of the imperfection anymore (see Fig. 6b). The chosen SEM spot is in the middle of the imperfection, so Figs. 11b and c show the repair coating in different magnifications. The type II-b sample shows, similar as the type II-a sample, a dense alumina film with excellent adhesion to the substrate, yet with an increased film thickness of about 8–9 µm as described within Fig. 6d. Sparse pores in nanometer range are visible on the right side of Fig. 11c. Nevertheless, the film can be considered gas-tight, as otherwise oxidation would have taken place (see Fig. 7).

The results clearly show the capability of PAD and µPAD to manufacture gas-tight ceramic protection films on substrates and preexisting coatings. Even for transitions from uncoated to previously coated areas as present in damaged surfaces, an additional passivation film is successfully applied. While µPAD seems to be limited in terms of deposition areas in the first place, and therefore in its repairing capabilities, the PAD feature of film growth on nearly any previous surface is the key for larger area processing. A mobile µPAD chamber can be placed anywhere on the flawed part as long as the chamber is closed hereby. Multiple spot-depositions with slightly overlapping coating areas enable the reprocessing of larger damaged regions, especially since coating durations per spot are quite short.

4. Conclusion

Repair instead of discard – following this motto, we propose the

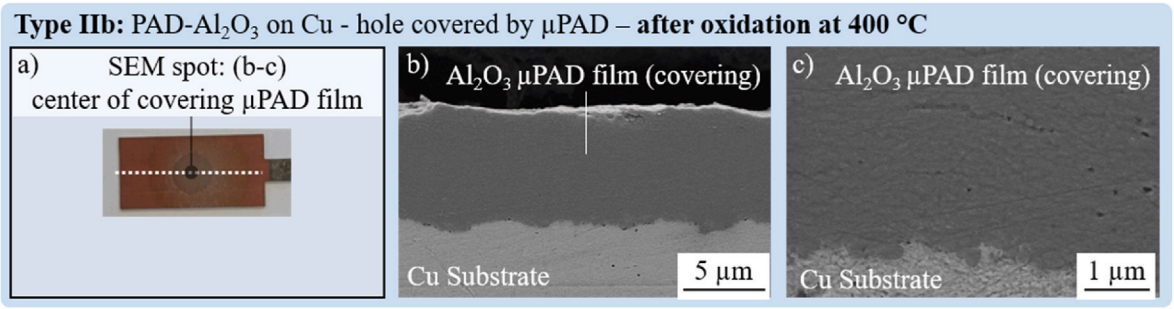

Fig. 11. A top view of the oxidized type II-b sample, marked with the SEM spot, is shown in a). Cross-sectional images, taken by SEM in different magnifications are shown in b) and c).

powder aerosol deposition as an application-oriented method to repair damaged coatings with ceramic films at room temperature. Initially, identical samples were prepared by coating blank Cu substrates with an artificial imperfection (a Kapton® masked artificially damaged spot) with alumina. Hereinafter, two different setups were used to repair the imperfection: a conventional PAD apparatus with a moving substrate holder and a slit nozzle as well as a µPAD apparatus with an immobile substrate holder and a de-Laval nozzle. Both setups for the repairing of damaged coatings comply with the requested film properties: a dense and well-adhering film, no matter whether the interface of the repair coating is the initial alumina film or the blank Cu from the imperfection. The quality of the repair coating is so high that no distinction can be made between it and the initial alumina film. Furthermore, crucial regions like the different height levels at the transition from the initial alumina layer to the hole were coated without suffering in terms of film quality.

While no differences between the PAD apparatuses can be found in terms of film quality, the shapes of the coatings are different. The conventional PAD adds a constant film thickness on top of the initial alumina film and the hole, therefore the surface of the repair coating resembles to the underlying structure. In contrast, the µPAD film thickness is bell-shaped. The artificially damaged spot disappears underneath it leaving an elevated, tableau-like repair coating.

Both repair coatings and an unrepaired sample underwent a heat treatment at 400 °C in oxidizing atmospheres in a muffle furnace. While the unrepaired artificially damaged spot oxidizes to CuO (black surface), both repaired samples show no signs of oxidization proving a gas-tight coating.

Summarizing the conducted experiments, the conventional PAD and the µPAD enable high quality films being suitable to repair damaged ceramic coatings at room temperature. The different apparatus types do not only enable to repair potentially large coating damages within the conventional PAD apparatus, but also demonstrate the mobile usage of the µPAD.

For future approaches, the direct implementation of a preceding cleaning treatment to remove oftentimes existing surface or film residues with low adhesion is of high interest, e.g. already formed copper oxides. This possibly can be achieved by using the µPAD device with a second aerosol container filled with coarse silica powders as utilized in sand blasting applications. Process parameters may be altered to support abrasion followed by an operation with solely carrier gas to remove the blasting material from the part's surface.

Author contributions

J.E. conceived, designed, and performed the experiments and subsequently analyzed the data and evaluated the results. T.N., M.L. and J.E. discussed the experimental design and all authors discussed the data jointly. J.K. and R.M. supervised the work. M.L., J.E. and R.M. wrote the paper. All authors have given approval to the final version of the manuscript.

Funding sources

Funding by the Deutsche Forschungsgemeinschaft (DFG, German Research Foundation) is gratefully acknowledged (491183248 and DFG grant MO 1060/40-1). Funded by the Open Access Publishing Fund of the University of Bayreuth.

Notes

The authors declare no competing financial interest.

Conflicts of interest

The authors declare no conflicts of interest.

Declaration of competing interestDoCI

The authors declare that they have no known competing financial interests or personal relationships that could have appeared to influence the work reported in this paper.

Acknowledgements

The authors are indebted to Mrs. Nicole Hall and the Bavarian Polymer Institute (KeyLab Electron and Optical Microscopy) for SEM imaging. Special thanks go to Philipp Nieke for the development and provision of the de-Laval nozzles.

References

[1] J.-P. Maria, X. Kang, R.D. Floyd, E.C. Dickey, H. Guo, J. Guo, A. Baker, S. Funihashi, C.A. Randall, Cold sintering: current status and prospects, J. Mater. Res. 32 (2017) 3205–3218, https://doi.org/10.1557/jmr.2017.262.

[2] D. Hanft, J. Exner, M. Schubert, T. Stöcker, P. Fuierer, R. Moos, An overview of the aerosol deposition method: process fundamentals and new trends in materials applications, J. Ceram. Sci. Technol. 6 (2015) 147–182, https://doi.org/10.4416/JCST2015-00018.

[3] J. Guo, R. Floyd, S. Lowum, J.-P. Maria, T. Herisson de Beauvoir, J.-H. Seo, C. A. Randall, Cold sintering: progress, challenges, and future opportunities, Annu. Rev. Mater. Res. 49 (2019) 275–295, https://doi.org/10.1146/annurev-matsci-070218-010041.

[4] J. Akedo, Aerosol deposition (AD) integration techniques and their application to microdevices, in: M. Singh, T. Ohji, R. Asthana, S. Mathur (Eds.), Ceramic Integration and Joining Technologies, John Wiley & Sons, Inc, Hoboken, NJ, USA, 2011, pp. 489–520.

[5] A. Vardelle, C. Moreau, J. Akedo, H. Ashrafizadeh, C.C. Berndt, J.O. Berghaus, M. Boulos, J. Brogan, A.C. Bourtsalas, A. Dolatabadi, M. Dorfman, T.J. Eden, P. Fauchais, G. Fisher, F. Gaertner, M. Gindrat, R. Henne, M. Hyland, E. Irissou, E. H. Jordan, K.A. Khor, A. Killinger, Y.-C. Lau, C.-J. Li, L. Li, J. Longtin, N. Markocsan, P.J. Masset, J. Matejicek, G. Mauer, A. McDonald, J. Mostaghimi, S. Sampath, G. Schiller, K. Shinoda, M.F. Smith, A.A. Syed, N.J. Themelis, F.-L. Toma, J.P. Trelles, R. Vassen, P. Vuoristo, The 2016 thermal spray roadmap, J. Therm. Spray Technol. 25 (2016) 1376–1440, https://doi.org/10.1007/s11666-016-0473-x.

[6] J. Exner, T. Nazarenus, J. Kita, R. Moos, Dense Y-doped ion conducting perovskite films of $BaZrO_3$, $BaSnO_3$, and $BaCeO_3$ for SOFC applications produced by powder

aerosol deposition at room temperature, Int. J. Hydrogen Energy 45 (2020) 10000–10016, https://doi.org/10.1016/j.ijhydene.2020.01.164.
[7] H. Kwon, Y. Kim, H. Park, C. Lee, The importance of intimate inter-crystallite bonding for the plasma erosion resistance of vacuum kinetic sprayed Y_2O_3 coating, Surf. Coating. Technol. 374 (2019) 493–499, https://doi.org/10.1016/j.surfcoat.2019.05.052.
[8] L.-S. Wang, H.-F. Zhou, K.-J. Zhang, Y.-Y. Wang, C.-X. Li, X.-T. Luo, G.-J. Yang, C.-J. Li, Effect of the powder particle structure and substrate hardness during vacuum cold spraying of Al_2O_3, Ceram. Int. 43 (2016) 4390–4398, https://doi.org/10.1016/j.ceramint.2016.12.085.
[9] D.-M. Chun, J.-O. Choi, C.S. Lee, S.-H. Ahn, Effect of stand-off distance for cold gas spraying of fine ceramic particles (<5μm) under low vacuum and room temperature using nano-particle deposition system (NPDS), Surf. Coating. Technol. 206 (2012) 2125–2132, https://doi.org/10.1016/j.surfcoat.2011.09.043.
[10] Y. Park, D.-S. Park, S.D. Johnson, W.-H. Yoon, B.-D. Hahn, J.-J. Choi, J. Ryu, J.-W. Kim, C. Park, Effect of gas flow rates and nozzle throat width on deposition of α-alumina films of granule spray in vacuum, J. Eur. Ceram. Soc. 37 (2017) 2667–2672, https://doi.org/10.1016/j.jeurceramsoc.2017.02.021.
[11] J. Akedo, Aerosol deposition of ceramic thick films at room temperature: densification mechanism of ceramic layers, J. Am. Ceram. Soc. 89 (2006) 1834–1839, https://doi.org/10.1111/j.1551-2916.2006.01030.x.
[12] H. Kwon, Y. Kim, H. Park, C. Lee, Impact behavior for successful particle–particle bonding in vacuum kinetic spraying, J. Therm. Spray Technol. 30 (2020) 542–557, https://doi.org/10.1007/s11666-020-01078-7.
[13] J. Akedo, Room temperature impact consolidation (RTIC) of fine ceramic powder by aerosol deposition method and applications to microdevices, J. Therm. Spray Technol. 17 (2008) 181–198, https://doi.org/10.1007/s11666-008-9163-7.
[14] J. Akedo, Room temperature impact consolidation and application to ceramic coatings: aerosol deposition method, J. Ceram. Soc. Jpn. 128 (2020) 101–116, https://doi.org/10.2109/jcersj2.19196.
[15] J.-J. Choi, J.-H. Lee, D.-S. Park, B.-D. Hahn, W.-H. Yoon, H.-T. Lin, Oxidation resistance coating of LSM and LSCF on SOFC metallic interconnects by the aerosol deposition process, J. Am. Ceram. Soc. 90 (2007) 1926–1929, https://doi.org/10.1111/j.1551-2916.2007.01641.x.
[16] J.-J. Choi, D.-S. Park, B.-D. Hahn, J. Ryu, W.-H. Yoon, Oxidation behavior of ferritic steel alloy coated with highly dense conducting ceramics by aerosol deposition, J. Am. Ceram. Soc. 91 (2008) 2601–2606, https://doi.org/10.1111/j.1551-2916.2008.02506.x.
[17] J.-J. Choi, J. Ryu, B.-D. Hahn, W.-H. Yoon, B.-K. Lee, D.-S. Park, Dense spinel $MnCo_2O_4$ film coating by aerosol deposition on ferritic steel alloy for protection of chromic evaporation and low-conductivity scale formation, J. Mater. Sci. 44 (2009) 843–848, https://doi.org/10.1007/s10853-008-3132-x.
[18] J.-J. Choi, J. Ryu, B.-D. Hahn, W.-H. Yoon, B.-K. Lee, J.-H. Choi, D.-S. Park, Ni-containing conducting ceramic as an oxidation protective coating on metallic interconnects by aerosol deposition, J. Am. Ceram. Soc. 93 (6) (2010) 1614–1618, https://doi.org/10.1111/j.1551-2916.2010.03646.x.
[19] H.S. Ryu, T.S. Lim, J. Ryu, S.-H. Hong, Corrosion protection performance of YSZ coating on AA7075 aluminum alloy prepared by aerosol deposition, J. Electrochem. Soc. 160 (2012) C42–C47, https://doi.org/10.1149/2.038302jes.
[20] N. Seto, K. Endo, N. Sakamoto, S. Hirose, J. Akedo, Hard α-Al_2O_3 film coating on industrial roller using aerosol deposition method, J. Therm. Spray Technol. 23 (2014) 1373–1381, https://doi.org/10.1007/s11666-014-0135-9.
[21] W.-H. Lee, H.-J. Kim, D.-W. Lee, M.-G. Jeong, D.-S. Lim, S.-M. Nam, Al_2O_3-nanodiamond composite coatings with high durability and hydrophobicity prepared by aerosol deposition, Surf. Coating. Technol. 206 (2012) 4679–4684, https://doi.org/10.1016/j.surfcoat.2012.05.052.
[22] S.D. Johnson, F.J. Kub, C.R. Eddy Jr., ZnS/Diamond composite coatings for infrared transmission applications formed by the aerosol deposition method, Proc. SPIE 8708 (2013) 87080T, https://doi.org/10.1117/12.2029717.
[23] P. Nieke, J. Kita, M. Häming, R. Moos, Manufacturing dense thick films of lunar regolith simulant EAC-1 at room temperature, Materials 12 (2019) 487, https://doi.org/10.3390/ma12030487.
[24] P. Fuierer, R. Calvo, G. Strobel, Dense, nano-grained, multi-phase ceramic coatings by dry aerosol deposition of lunar regolith simulant, Addit. Manuf. 35 (2020) 101304, https://doi.org/10.1016/j.addma.2020.101304.
[25] M. Suzuki, T. Tsuchiya, J. Akedo, Effect of starting powder morphology on film texture for bismuth layer-structured ferroelectrics prepared by aerosol deposition method, Jpn. J. Appl. Phys. 56 (2017), 06GH02, https://doi.org/10.7567/JJAP.56.06GH02.
[26] J. Exner, M. Schubert, D. Hanft, J. Kita, R. Moos, How to treat powders for the room temperature aerosol deposition method to avoid porous, low strength ceramic films, J. Eur. Ceram. Soc. 39 (2019) 592–600, https://doi.org/10.1016/j.jeurceramsoc.2018.08.008.
[27] P. Sarobol, M. Chandross, J.D. Carroll, W.M. Mook, D.C. Bufford, B.L. Boyce, K. Hattar, P.G. Kotula, A.C. Hall, Room temperature deformation mechanisms of alumina particles observed from in situ micro-compression and atomistic simulations, J. Therm. Spray Technol. 25 (2016) 82–93, https://doi.org/10.1007/s11666-015-0295-2.
[28] S. Kuroyanagi, K. Shinoda, A. Yumoto, J. Akedo, Size-dependent quasi brittle–ductile transition of single crystalline alpha-alumina particles during microcompression tests, Acta Mater. 195 (2020) 588–596, https://doi.org/10.1016/j.actamat.2020.05.065.
[29] D.R. Patil, V. Annapureddy, J. Kaarthik, A. Thakre, J. Akedo, J. Ryu, Piezoelectric thick film deposition via powder/granule spray in vacuum: a review, Actuators 9 (2020) 59, https://doi.org/10.3390/act9030059.
[30] H. Palneedi, I. Choi, G.-Y. Kim, V. Annapureddy, D. Maurya, S. Priya, J.-W. Kim, K. J. Lee, S.-Y. Choi, S.-Y. Chung, S.-J.L. Kang, J. Ryu, D. Vieland, Tailoring the magnetoelectric properties of $Pb(Zr,Ti)O_3$ film deposited on amorphous metglas foil by laser annealing, J. Am. Ceram. Soc. (2016) 1–8, https://doi.org/10.1111/jace.14270.
[31] J. Exner, M. Linz, J. Kita, R. Moos, Making Powder Aerosol Deposition accessible for small amounts: a novel & modular approach to produce dense ceramic films, Int. J. Appl. Ceram. Technol. (2021) 2178–2196, https://doi.org/10.1111/ijac.13841.
[32] M. Linz, J. Exner, J. Kita, F. Bühner, M. Seipenbusch, R. Moos, Discontinuous powder aerosol deposition: an approach to prepare films using smallest powder quantities, Coatings 11 (2021) 844, https://doi.org/10.3390/coatings11070844.
[33] M. Lebedev, S. Krumdieck, Optically transparent, dense α-Al2O3 thick films deposited on glass at room temperature, Curr. Appl. Phys. 8 (2008) 233–236, https://doi.org/10.1016/j.cap.2007.10.057.
[34] H.J. Lee, J. Yu, Study on the effects of copper oxide growth on the peel strength of copper/polyimide, J. Electron. Mater. 37 (2008) 1102–1110, https://doi.org/10.1007/s11664-007-0317-z.